Title
Cloud base height from sky imager and cloud speed sensor

Authors
Wang, Guang
Kurtz, Ben
Kleissl, Jan

Publication Date
2016-06-01

DOI
10.1016/j.solener.2016.02.027

Cloud base height from sky imager and cloud speed sensor

Guang Wang, Ben Kurtz, Jan Kleissl
Center for Renewable Resources and Integration, Department of Mechanical and Aerospace Engineering, University of California, San Diego, United States

Abstract

Cloud base height (CBH) is a critical input to short-term solar forecasting algorithms, yet CBH measurements are difficult to obtain. Existing methods to detect CBH include radiosondes, ceilometers, and the stereographic method. However, these methods are deficient for intra-hour forecasting due to high costs or low temporal resolution. While satellite images could overcome these limitations, only the cloud top height can be determined from the thermal IR channel. We describe the integration of a cloud shadow speed sensor (CSS) with angular cloud speed from a sky imager to determine CBH. Furthermore, an improved methodology to determine cloud motion vectors from the CSS is presented, which offers lower noise and greater accuracy and stability than existing methods. Two months at the UC San Diego campus were used for validation against measurements from meteorological aerodrome reports (METAR) and an on-site ceilometer. Typical daily root mean square differences (RMSD) are 126 m which corresponds to 16.9% of the observed CBH. Normalized RMSD remains below 30% for all days. The daily bias is usually less than 80 m which suggests that the method is robust and that most of the RMSD is driven by short-term random fluctuations in CBH. Unlike sky image stereography the present method can be applied to measurements at a single site making it widely applicable.

Nomenclature

Note that Δt_{ij} and ϕ_{ij} are used with subscripts when referring to a particular sensor pair and without subscripts when referring to a continuous functional fit of the time shift. Also generally *v* denotes a vector and *U* denotes a scalar cloud speed. Unless explicitly noted here and in the text for cloud pixel speeds, all cloud speeds have units of m s^{-1}.

θ_m	Sky imager field of view in degrees from the vertical	MCP	Most correlated pair method for cloud speed measurement
θ_{sensor}	Angle offset between sensors on the CSS	n	Number of pixels of the cloud map in one dimension
β	Direction of v_{real} in reference to line (a-c) of CSS	N	Total number of data points
$\phi_\perp$	Direction of $v_\perp$ in reference to line (a-c) of CSS	nRMSD	Normalized root mean square difference
ϕ_{ij}	Angle between the line connecting sensors i and j and line (a-c) of CSS	p_k	Sensor pair number
Δt_{ij}	Time shift of cloud arrival time between CSS sensors i and j	r	Radius of the CSS sensor circle
AGL	Above ground level	R_{ij}	Maximum cross-correlation coefficient of sensor pair i – j
AMSL	Height above mean sea level (m)	RMSD	Root mean square difference
CBH_{ceilo}	CBH estimates from the ceilometer	U_{CSS}	CSS cloud speed
$CBH_{CSS+USI}$	CBH derived from CSS cloud speed and USI cloud pixel speed	U_{pixel}	Cloud pixel speed
CBH	Cloud base height	U_{USI}	USI derived cloud speed
CMV	Cloud motion vector	USI	UC San Diego Sky Imager
CSS	Cloud Shadow Speed Sensor	v_{real}	True cloud velocity vector
LCE-CFM	Linear Cloud edge – Curve Fitting Method	$v_\perp$	Component of v_{real} perpendicular to the

cloud edge

1. Introduction

Cloud base height (CBH) plays an important role in many solar energy applications. For example, Bright et al. (2015) incorporate CBH to generating synthetic irradiance signals. While an accurate source of CBH become less critical in larger-scale forecasting such as satellite image based forecasting, it does matter in short-term solar forecasting which is becoming vital in the solar industry as solar penetration increases (Yang et al. 2014). As the cloud is observed by the sky imager, variations in CBH change the distance between the latitude and longitude of the center of the cloud and its shadow on the ground. In addition the physical cloud size (and its shadow size) scales linearly with CBH. Hence, incorrect CBHs lead to offsets between modeled and actual cloud shadow. In addition, inaccurate cloud speed associated with CBH errors causes errors in the estimated arrival time of cloud shadows, which leads to offsets in ramp forecasting.

The most common CBH measurement techniques include radiosondes (Wang and Rossow, 1995) and ceilometers (Gaumet et al. 1998; Martucci et al. 2010). A radiosonde is a battery-powered telemetry instrument package that vertically profiles the atmosphere. Although the measurement is accurate as it is taken in-situ, the observations are usually taken only twice daily at major airports. This frequency is not sufficient for intra-hour forecasting. Ceilometers, as the most common CBH observational tool, emit a high intensity near-infrared laser beam vertically. A vertical profile of atmospheric backscatter is then obtained and CBH can be computed multiple times per minute. Ceilometer CBH measurements are usually reported in meteorological aerodrome reports (METAR). While METAR stations report high quality CBH data, limited temporal resolution (hourly reports) and spatial heterogeneity in cloud cover and CBH, can cause differences between METAR and local CBH. Since the cost of ceilometers is relatively high, their application outside of airports is limited in most countries, although ceilometers are standard at weather observation stations in the UK.

A few indirect methods of CBH estimation have emerged during the past decade. Killius et al. (2015) estimate CBH based on the output of a Numerical Weather Prediction model. CBH estimates with ground based infrared measurements (Shaw and Nugent, 2013; Liu et al. 2015) were developed based on the monotonic relationship between CBH and downwelling thermal infrared radiance. The assumption that clouds are blackbodies leads to an over-estimation of the CBHs derived by infrared cloud imagers (Liu et al. 2015). Satellite images (Prata and Turner, 1997; Dessler et al. 2006) estimate cloud height with great spatial coverage and resolution, but the fact that satellite radiance is primarily a function of cloud top height limits its application in short-term solar forecasting. The stereographic method using two or more sky imagers was initially proposed by Allmen and Kegelmeyer (1996) and refined by Kassianov et al. (2005). Nguyen and Kleissl (2014) further improved stereographic CBH detection and determined CBH using a two-dimensional (2D) method for single homogeneous cloud layers and an enhanced three-dimensional (3D) method to provide CBH with high spatial resolution. However, the stereographic method requires two sky imagers spaced 1.23 km apart and accurate geometric calibration of the imaging systems is critical (Urquhart et al. 2015).

The cloud shadow speed sensor (CSS) (Fung et al. 2014) or cloud speed measurements from spatially distributed irradiance or power sensors within a power plant (Bosch and Kleissl, 2013) offer an alternative to direct CBH measurements when combined with a sky imager. Since the cloud pixel speed (or angular cloud speed) determined by the sky imager can be expressed as the ratio of cloud speed [m s^{-1}] and CBH, CBH can be computed from collocated sky images and cloud motion vectors (CMVs). Hence, accurate CMV estimation is critical to CBH computation. While existing CMV methodology was proposed by Bosch et al. (2013), we present an enhanced CMV methodology that is more suitable for CBH computation. Some limitations of the approach and validation should be disclosed upfront. The CMV as derived from the CSS applies to the cloud edge approaching the sun, but cloud pixel speed is determined in the entire field of view of the sky imager, resulting in inconsistency in CBH computation. Furthermore, the ceilometer measurement used for validation presents temporally averaged CBH at zenith (versus at solar zenith for the CSS). Therefore, random differences between computed CBH and ceilometer CBH are expected for validation, but biases should be small.

The principal objective of this paper is to propose a method that offers an accurate local CBH for sky imager solar forecasting. This method incorporates a cloud speed sensor with an enhanced algorithm to a sky imager, and the package provides an affordable and convenient approach to estimate CBH compared to a ceilometer. This paper is organized in five sections. The UCSD CSS and data availability will be described in Section 2. A new algorithm to derive cloud speed from CSS raw data is described in Sections 3.1 and 3.2. Sections 3.3 and 3.4 introduce a method that combines CSS and UCSD sky imager (USI) results to determine CBH. Section 4 provides CBH validation against an on-site ceilometer. Section 5 provides conclusions on the method, applications, and future work.

2. Hardware

2.1 Instrumentation and setup

The CSS (Fung et al. 2014) is a compact system that measures cloud shadow motion vectors (CMVs). The system offers an affordable technique to measure CMVs with material costs of less than US$400. It consists of an array of eight satellite phototransistors (TEPT4400, Vishay Intertechnology Inc., USA) positioned around an identical phototransistor located at the center of a half circle of radius 0.297 m, covering 0-105° in 15° increments (Fig. 1). The sensors have a spectral response ranging from approximately 350 to 1000 nm with peak sensitivity at 570 nm. Sensor response time was determined experimentally in a laboratory controlled environment and was found to be 21 µs rise time (10 - 90% response). High-frequency irradiance data are taken from all sensors and fed to a microcontroller (chipKIT Max32, Digilent Inc., USA). The on-board static memory allows fast storage of 6,000 10-bit data points per cycle. Due to the high sampling frequency, the measurements are not continuous. With the sampling rate of 667 samples s^{-1}, 6,000 data points fill up the on-board memory in approximately 9 sec. These 9 sec of data are then processed to determine one CMV as described in Section 3. During this process, the raw data collection has to be temporarily suspended for about 9 sec resulting in a temporal resolution of CMVs of about 18 sec. The CMVs used in this analysis were taken from a CSS located at 32.8810°N, -117.2328°W, and 106 m height above mean sea level (AMSL) (marked as CSS in Fig. 2).

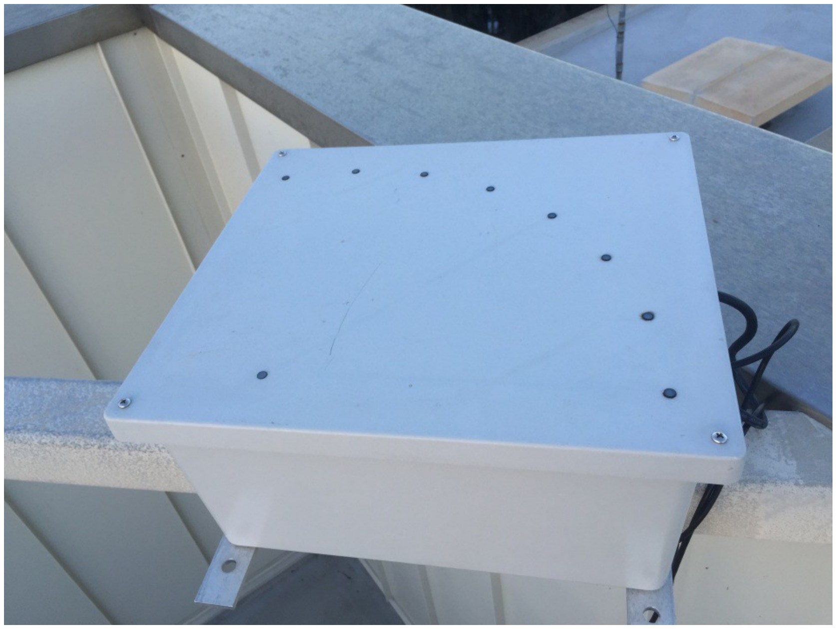

Fig. 1: Cloud Shadow Speed Sensor (CSS) contained inside a weather-proof enclosure with dimensions 0.45 x 0.40 m. On the top of the enclosure is an array of nine phototransistors.

Sky images were taken every 30 sec by a USI located at 32.8722°N, -117.2409°W, 129 m AMSL (marked as USI1_2 in Fig. 2). The USI is designed and developed for short-term solar forecasting applications (Urquhart et al. 2015). It features a high quality imaging sensor and lens contained in a thermally controlled and compact environmental housing. The capture software is employed with a high dynamic range (HDR) imaging technique. Independent measurements of CBH were taken by a Vaisala CT25K ceilometer co-located with the CSS. While all sensors report CBH above ground level (AGL), the elevation of the sensor was added to obtain CBH (AMSL).

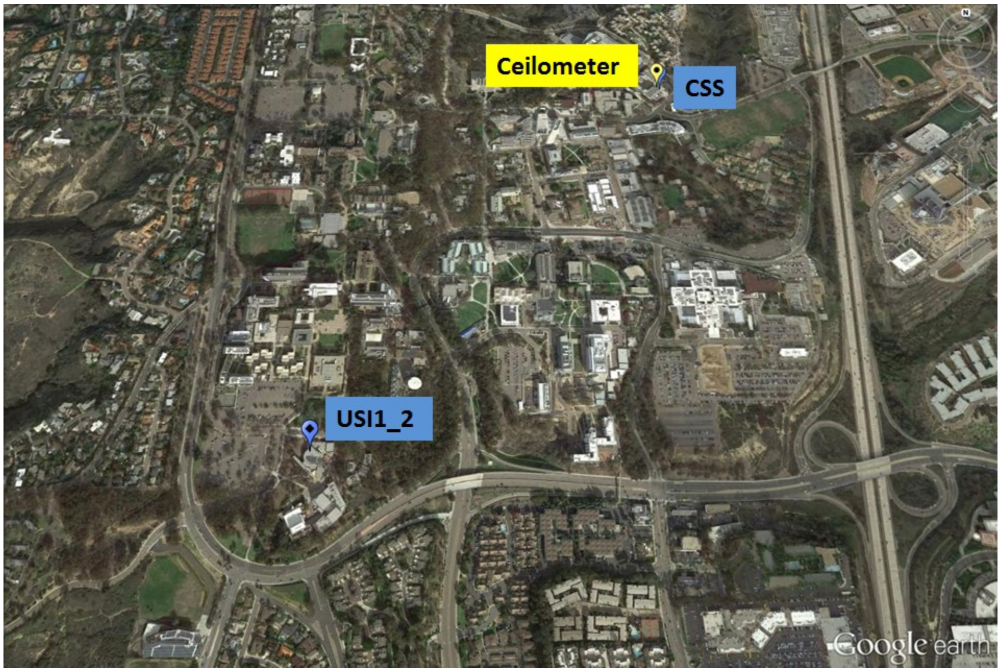

Fig. 2: Locations of sky imager (USI1_2), ceilometer and Cloud Shadow Speed Sensor (CSS) on the UCSD campus. The straight-line distance between USI and CSS is 1.25 km. Map data ©2015 Google.

2.2 Data availability

Since USI data was available continuously, data availability was restricted by the CSS and ceilometer's operational availability. The CSS was setup on Apr 4 2015. However; intermittent technical issues occurred until May 1, 2015, when it became fully operational. In order to comprehensively assess the performance of the CSS during a variety of sky conditions, April 5, April 20, and the period of May 1 through July 29 were selected for analysis. During this period, 35 of 92 days were clear or contained less than 4 hours of cloud cover per day, and there were 21 overcast or rainy days. Because clear and overcast days do not produce nearly as many ramp occurrences as partly cloudy days, our study rejects the days with clear or overcast conditions. Nine additional days had to be eliminated due to missing ceilometer measurements. The remaining 27 days contain partial cloud cover for at least 4 hours (except July 1 which contains unusually high clouds for the southern California region which lasted for 2 hours), which are the conditions of interest for testing CSS performance.

3. Cloud Speed Measurements

3.1 Prior cloud speed sensor algorithm: Most Correlated Pair Method (MCP)

While the method of determining CBH is compatible with any measurement of cloud speed, we also present a new method to obtain cloud speed from the CSS as it had not been documented before. In the prior CSS algorithm proposed by Bosch et al. (2013), the CMVs were determined by the Most Correlated Pair Method (MCP). MCP assumes that due to heterogeneity in the cloud shadow over the area of the sensor, the pair of sensors that lie along the direction of cloud motion will experience the largest cross-correlation as they see the same transect of the cloud (Bosch et al. 2013). Thus, the pair with the largest cross-correlation coefficient is therefore used to determine the direction of cloud motion. The time shift of maximum cross-correlation between the selected pair is then used to calculate the cloud speed. The MCP method suffers from some deficiencies. Most importantly, for the ideal case of a linear cloud edge separating shadow from clear sky, each sensor would see exactly the same signal shape and there would be no single most correlated pair. Instead, the most correlated pair would simply result from arbitrary correlations from sensor noise. Scenarios close to this idealization were found to be common. Since clouds are typically much larger than the spacing between sensors, it seems intuitive that the cloud is nearly homogeneous over the area of the CSS. Thus, CMV results were highly variable. Bosch et al. (2013) addressed the variability through statistical post-processing to determine the most common cloud direction and corresponding cloud speed. The post-processing was shown to be robust and accurate, but the temporal averaging reduced the response of the sensor to sudden changes in cloud velocity. The MCP method also had limited precision as the final direction could only be along individual sensor pairs.

3.2. Improved cloud speed sensor algorithm: Linear Cloud Edge – Curve Fitting Method (LCE-CFM)

The assumption in the MCP method is modified to enhance the accuracy and robustness of the method in an operational environment. Because the CSS is small compared to a typical cloud, we can reasonably assume the cloud edge to be linear (Fig. 3). The signal measured by each sensor is then identical except of the temporal deviation between the signals, resulting in a perfect cross-correlation $R_{ij}=1$ (i and j refer to the sensors). Therefore, it is not the magnitude of the cross-correlation that distinguishes the sensor pair aligned with the CMV, rather the time lag associated with the maximum R_{ij} between different sensor pairs provides clues as to the relative alignment of each pair with respect to the CMV. Hence, we will fit a function to the time lag versus sensor-pair direction, and we term this method the “Linear Cloud Edge – Curve Fitting Method”.

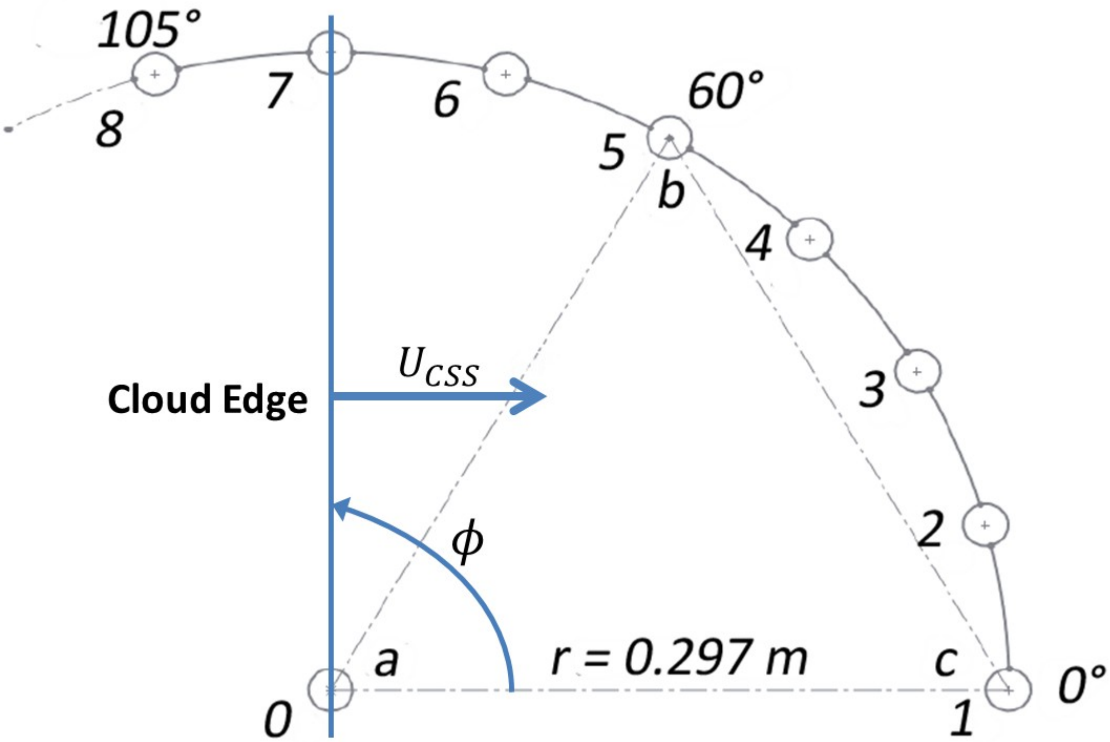

Fig. 3: Illustration of the linear cloud edge assumption and LCE-CFM method on top of the CSS luminance sensor arrangement. Each circle represents a sensor arranged in a circular pattern with 15° spacing about the central sensor. The sensor pair combinations are constructed with the central sensor and one of the other sensors for angles from 0° to 105°, e.g., sensor pair combination 0/1 for 0°, 0/2 for 15°, etc. Additional angles from 120° to 165° are obtained through equilateral triangles between the central sensor and another sensor pair, e.g., sensor pair combination 1/5 for 120°, 2/6 for 135°, etc. The linear cloud edge is shown as a blue line and is assumed (for simplicity, but not limiting generality) to be advected along the line connecting sensors 0 and 1.

As in the MCP method, the maximum cross-correlation coefficient R_{ij} of each pair of signals will be determined (Fung et al. 2014) and the associated time shift Δt_{ij} for that pair will be recorded. Considering a linear cloud edge that is crossing the CSS moving in the direction of the sensor line (a-c), it is straightforward that:

$$r \cdot \cos\phi_{ij} = U_{CSS} \cdot \Delta t_{ij} \quad , \qquad (1)$$

where r is the radius of the sensor circle, ϕ_{ij} is the cloud edge direction that is defined as the angle between the line connecting sensors i and j and the line (a-c). i and j vary from 0 to 8, but only 12 sensor pair combinations i / j (0/1, 0/2, 0/3, 0/4, 0/5, 0/6, 0/7, 0/8, 1/5, 2/6, 3/7, 4/8) are used in our configuration. ϕ_{ij} can be expressed as (

$360^\circ - p_k \times 15^\circ$) where p_k is the sensor pair number (k = 0 to 11 following the brackets in the previous sentence). U_{CSS} is the speed of the cloud edge, i.e. cloud speed. With distance r and cloud speed U_{CSS} being constant for each pair, the time shift Δt_{ij} becomes a function of $\cos\phi_{ij}$. The trigonometric relation holds for all cloud edge directions as the cloud velocity is assumed to be perpendicular to the cloud edge. For the sensor pairs without the central sensor, Eqn. 1 still holds as long as the selected sensor i and the sensor j lie on one side of an equilateral triangle constructed from the central sensor, sensor i and sensor j . Because the time shift Δt_{ij} returned by the CSS can be either positive or negative depending on the cloud direction, 12 sensor pairs are sufficient to cover 360° in 15° increments.

For the ideal assumption of a linear cloud edge, plotting Δt versus ϕ would therefore be expected to produce a cosine function. For verification, the cosine function is used to fit the Δt_{ij} versus ϕ_{ij} points for each 9 sec measurement, and the R^2 value is employed to determine the goodness of the fit (Fig. 4). A high R^2 supports the linear cloud edge assumption. Since the linear cloud edge assumes that the velocity is perpendicular to the cloud edge, the sensor pair aligned with the CMV is farthest apart along the CMV at distance r . Thus, the maximum of the cosine function which represents the longest time shift Δt should occur at the CMV direction. While the side effect of LCE assumption is not explicitly visible in the results, the potential limitation and future improvement of LCE assumption are discussed in section 4.3. The cloud speed then becomes the ratio of the distance r and the time shift Δt :

$$U_{CSS} = \frac{r}{\Delta t} \quad . \qquad (2)$$

Note that the cosine model fit to Eqn. 1 should be constrained to return solutions with $\Delta t > 0$. Fig. 4 illustrates this procedure using 9 sec of luminance data. The correlations between all sensor pairs are very large (>0.999), which causes issues in the robustness of the MCP method. On the other hand, the linear cloud edge assumption is validated through a high R^2 value (0.99) which indicates that the time shift is indeed a strong function of the cosine of the direction. As a result the CMV direction and speed can be obtained with confidence using Eqn. 2.

In the example in Fig. 4 the time shift is determined as $\Delta t = 0.104$ s, and the corresponding direction is □ = 323° yielding a cloud speed U_{CSS} = 2.87 m s^{-1} as per Eqn. 2.

A filter is applied for data quality control: If the average R_{ij} is less than 0.9 or R^2 of the cosine curve fit is less than 0.9, the CMV will not be computed. Small R_{ij} is likely a result of no cloud passage or dynamic clouds. A small R^2 indicates poor curve fitting and therefore an unreliable result. Generally partly cloudy conditions result in numerous valid CMVs while homogeneous cloud conditions (e.g., clear and overcast) result in infrequent valid CMV output due to small R_{ij}. Typically, 1700 raw data sets are recorded during an eight hour analysis day, and about 110 CMVs are delivered for an overcast day and less than 10 CMVs for a clear day. For partly cloudy days, about 400 CMVs pass the quality control, which is equivalent to one CMV value every 50 sec. The sampling rate is sufficient for cloud motion estimation.

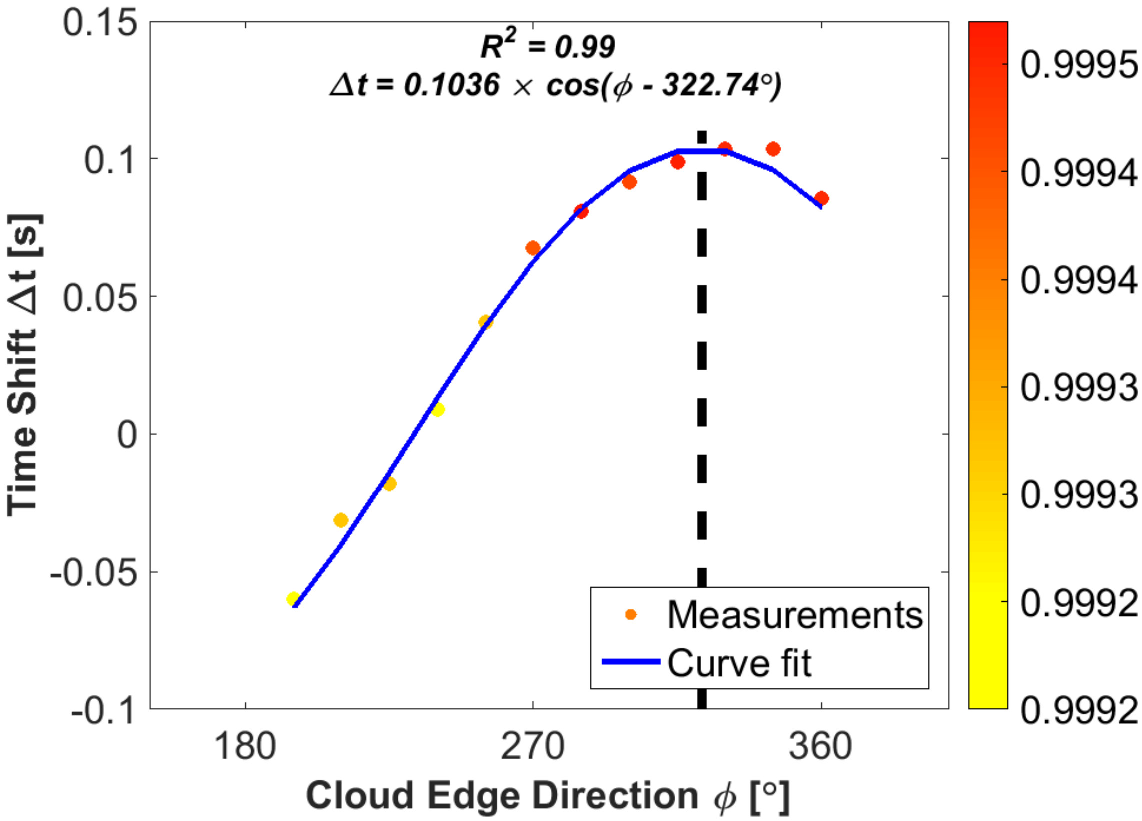

Fig. 4: Illustration of the LCE-CFM to determine CMVs on May 31, 2015 at 17:16:19 UTC. The *x*-axis represents direction ϕ that is equal to ($360° - p_k \times 15°$), where p_k is the sensor pair number (

k = 0 to 11). The *y*-axis represents the time shift Δt, and the color indicates the strength of correlation R_{ij}. The curve indicates the best fit of $\Delta t = 0.103 \times \cos\left(\phi - 322.7\,°\right)$. The maximum time shift of the cosine function is selected as the direction of cloud motion as indicated by the vertical dashed black line.

Fig. 5 shows a set of CMVs for one day together with filtered CMV direction determined by the USI as an independent validation. Clouds are moving northward at 1 to 6 m s^{-1} changing to eastward as the day progresses. The USI direction generally falls in the center of the CSS raw data points indicating good agreement. There is some variability in CSS raw data, which is likely a result of both physical cloud dynamics and sensor noise. The same trends are seen in the wind-rose plot for CSS data on this day in Fig. 6; most of CMVs cluster in the north-east-ward direction with an average speed range of 2 to 6 m s^{-1}. Additional validation of the LCE assumption is presented in Appendix A1.

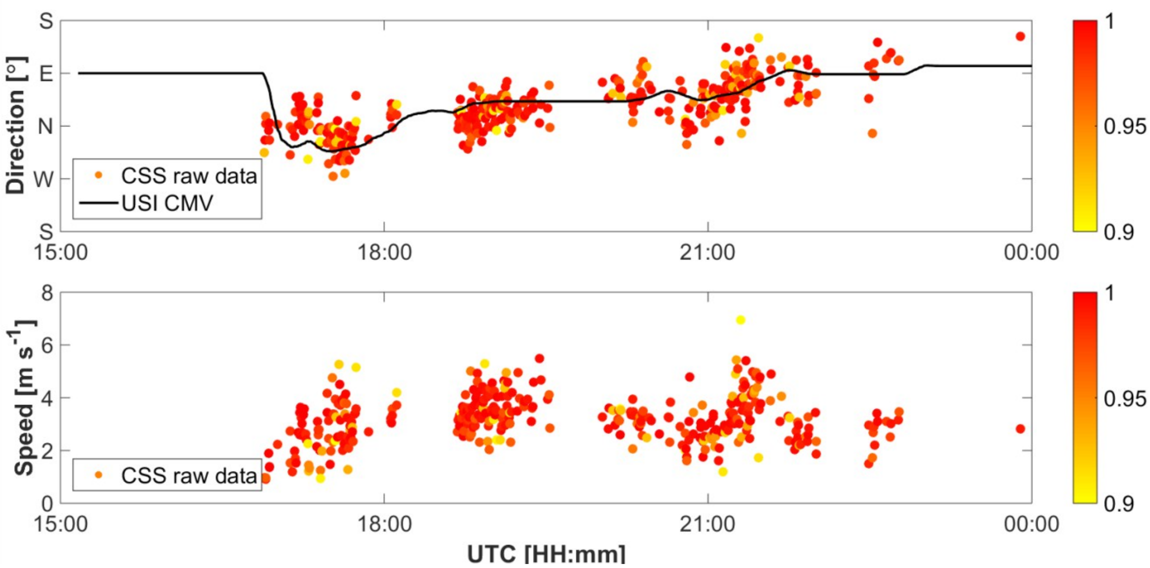

Fig. 5: Cloud direction (defined as direction the cloud is moving towards) and cloud speed determined by the LCE-CFM using CSS data on May 31, 2015. Each circle represents one CMV computed based on 9 seconds of measurements and the color provides the R^2 value for the curve fit of 9-second measurements. The black line presents an independent validation of cloud direction using the CMV determined from the USI. Since cloud speed in m s^{-1} cannot be determined from the USI alone, there is no validation data is in the lower graph.

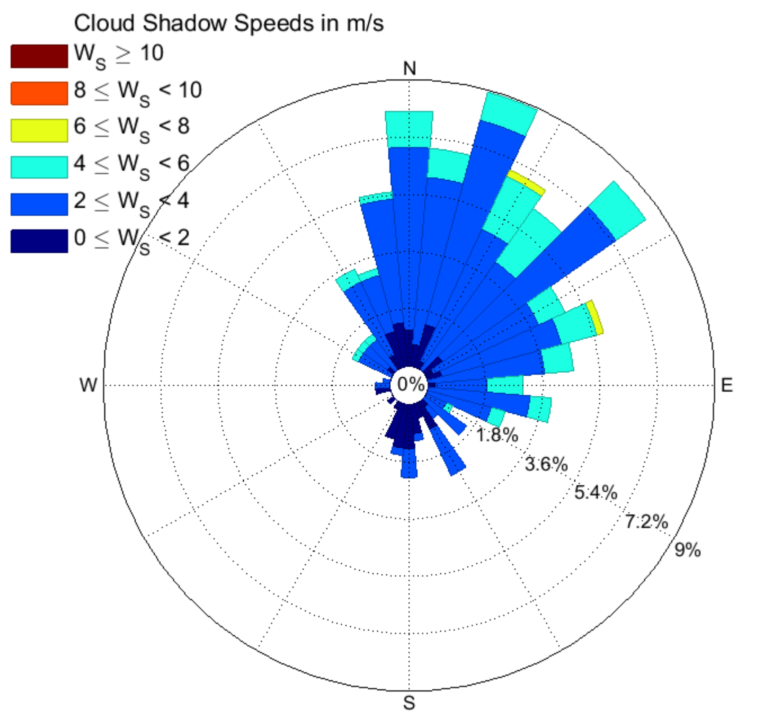

Fig. 6: Wind-rose plot of cloud direction and cloud speed of the data shown in Fig. 5. The color bins show cloud speed range, and the values on concentric circles represent the frequency of appearance of each cloud speed bin.

In summary, compared to the prior MCP method, the LCE-CFM yields two distinct advantages: (i) more clustered, i.e. robust, CMV results without post-filtering, and (ii) continuous cloud direction output compared to the 15° (equivalent to the angular arrangement of the sensors) discretized output for the MCP method. To demonstrate the improvement of the LCE-CFM, an example of the prior MCP method is provided in Appendix A2. The disadvantage is that the LCE-CFM calculates correlation for all sensor pairs, whereas the MCP method can bypass the calculation for poorly correlated pairs. This triples the computational time on the CSS microcontroller to 40 sec. Therefore, for this application, the processing was performed on a remote Intel I5 workstation instead, which decreases computational time by more than an order of magnitude.

3.3 Cloud pixel speed from USI data

In this section, we will first introduce the sky imager cloud motion algorithm, and based on that in conjunction with the CSS cloud speed, a local CBH will be determined. The USI can be used to detect clouds and obtain cloud pixel speed. These measurements yield forecasts of future cloud locations at high spatial and temporal resolutions and can improve forecast skill up to a 20 min forecast horizon. The benefit of using sky imager observations over a large ground sensor network is that only one or a few instruments deployed around the area of interest are capable of determining the current distribution of cloud cover at a high resolution. The forecast procedure is outlined in the flow chart in Fig. 7. The USI forecast procedure is briefly explained within this section. It is very similar to other standard forecast procedures, such as those presented by Cazorla Cabrera (2010) and Schmidt et al. (2015). For more details on the USI forecast, consult Chow et al. (2011), Ghonima et al. (2012), and Yang et al. (2014).

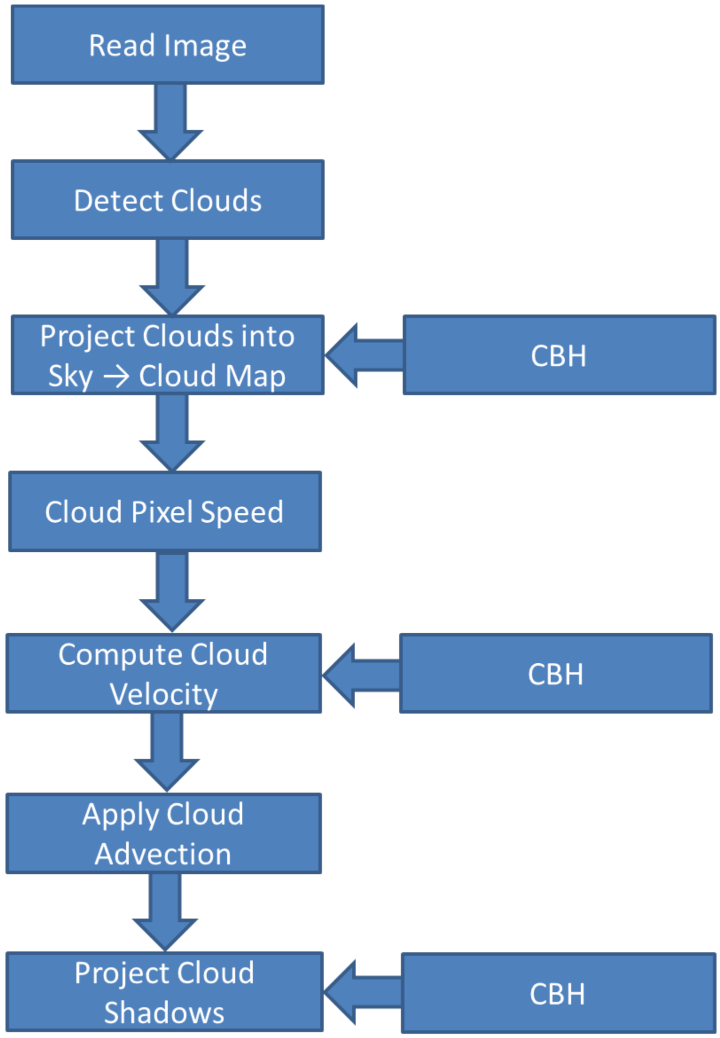

Fig. 7: Flowchart of the sky imager solar forecast procedure. CBH is used to project clouds onto a cartesian sky coordinate system, to obtain cloud speed, and to project the advected cloud shadows to the ground.

Cloudy pixels are detected using spectral information from the RGB images. CBH is then used in conjunction with lens geometry to map these clouds to a latitude-longitude grid at the CBH creating the cloud map (Chow et al. 2011). In absence of local data, CBH is taken from the closest METAR. Cloud pixel velocity is obtained by applying the cross-correlation method (CCM, Chow et al. 2011) to the RBR of two consecutive cloud maps. The cloud velocity [m s^{-1}] is then calculated by converting from cloud pixel speed [pixel s^{-1}] to cloud shadow speed using a velocity scaling factor which is a function of CBH (see Eqn. 3 later). Note that since the distance from sun to earth is much larger than the distance from cloud to earth, the cloud shadow speed is assumed to equal the cloud speed for all solar zenith angles.

3.4 Cloud base height determination from CSS and USI (CSS+USI method)

In this section, we introduce the mathematical algorithm (CSS+USI) that obtains the CBH for sky imager forecasting from CSS cloud speed measurements. Fig. 8 introduces the geometrical terms on a cloud map. In the USI forecast, cloud velocity is calculated by converting from cloud pixel speed to equivalent m s^{-1} cloud speed as:

$$U_{USI}=U_{pixel}\times\frac{CBH\times 2\tan\theta_m}{n}\quad, \tag{3}$$

where U_{USI} is cloud speed in units of m s^{-1} and U_{pixel} is image-average cloud pixel speed in units of pixel s^{-1} obtained through the cross-correlation method applied to two consecutive USI images. The last term in Eqn. 3 represents a velocity scaling factor, in which θ_m is the maximum view angle of the USI measured from zenith (here $\theta_m=80°$), $CBH\times 2\tan\theta_m$ is the horizontal length of the sky imager view domain (termed "cloud map"), and n is the number of pixels of the cloud map in one dimension (Fig. 8). Therefore, the velocity scaling factor has units of m pixel^{-1}. Note that the pixel size of the cloud map is distinct from the pixel size in the original sky image.

In Fig. 8, the cloud observed by the USI moves from time $t=t_0$ to $t=t_1$ and U_{pixel} is computed from the number of pixels that the cloud moves during the period t_1-t_0. The cloud map consists of n x n pixels, i.e. n is the number of pixels of the cloud map in one dimension. Its physical size is computed with the trigonometric expression $CBH\times 2\tan\theta_m$. So the term $\frac{CBH\times 2\tan\theta_m}{n}$ refers to the physical distance per pixel of the cloud map. With the cloud speed expressed as the number of pixels per second, U_{USI} can be calculated according to Eqn. 3.

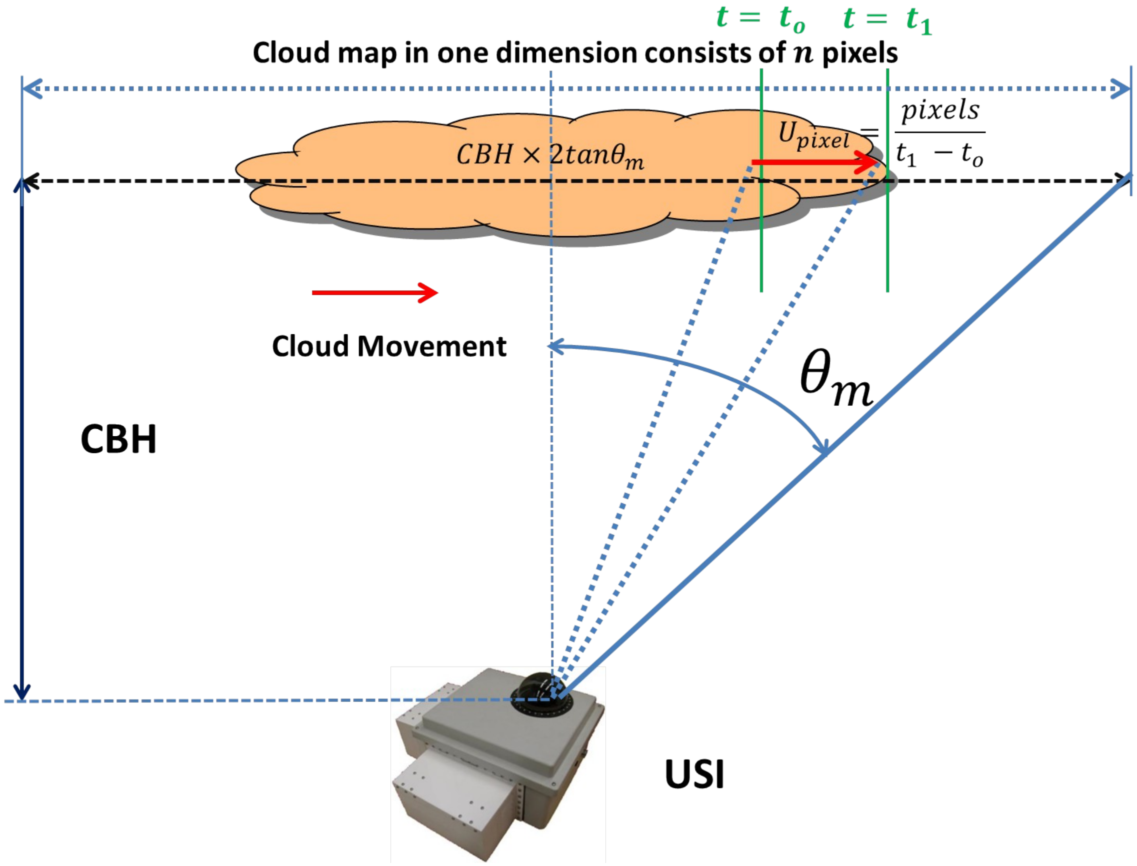

Fig. 8: Illustration of the geometrical and kinematic relations between cloud pixel speed U_{pixel}, cloud speed determined by USI U_{USI}, maximum view angle of the USI θ_m and CBH.

Eqn. 3 indicates how to obtain cloud speed in [m s^{-1}] from CBH and the USI derived cloud pixel speed. Conversely, with independent measurements of cloud speed from the CSS, U_{CSS}, we can back-calculate the local CBH (labeled as $CBH_{CSS+USI}$) by replacing U_{USI} with U_{CSS} in Eqn. 3 to yield:

$$CBH_{CSS+USI} = \frac{U_{CSS}}{U_{pixel}} \times \frac{n}{2\tan\theta_m} \quad . \tag{4}$$

It can be observed that CBH depends on the ratio of U_{CSS} and U_{USI}. Eqn. 4 is implemented into the USI forecast algorithm to calculate local CBH at each step using the most recent CSS measurement. The method is called CSS+USI and the detailed pseudocode and a flowchart of the method are available in Appendix A3.

A 10 min window median filter was applied to the time series of CBH from the CSS+USI method. Due to the small sampling area (a small cone above the ceilometer), heterogeneous cloud shapes, and cloud formation and movement, the raw 20 sec ceilometer data is too variable and is not representative of the CBH in the field of view of the USI. Therefore, consistent with Nguyen and Kleissl (2014) when the CSS+USI method yields a $CBH_{CSS+USI}$ at the USI timestamp, a 15 minute median filter centered on that timestamp is applied to ceilometer measurement. In this way, only the dominant ceilometer cloud layer is captured to compare with the filtered results of the proposed CSS+USI method.

4. Cloud base height validation

4.1 Aggregate CBH statistics

The CBH validation is presented in this section. The CSS+USI method is validated against METAR and an on-site ceilometer on the available days listed in Table 1. Two error metrics were used to characterize the performance of the method: root mean square difference (RMSD) and normalized RMSD.

$$RMSD=\sqrt{\frac{1}{N}\sum_{k=1}^{N}\left(CBH_{CSS+USI}-CBH_{ceilo}\right)^2}\ , \quad (5)$$

where N is the total number of data points. RMSD is divided by the daytime average CBH to obtain the normalized RMSD (nRMSD). Note that although both RMSD and nRMSD are used to evaluate the method, RMSD is relevant for the correct prediction of the timing of a ramp event.

The performance of the proposed method is summarized in Table 1 and Fig. 9 for a range of cloud types, cover fractions, heights, and layers that existed on these days. Generally low cumulus and low stratus clouds prevailed, but high cirrus clouds were observed on July 1, and May 22 featured altocumulus clouds. The best performance occurred on July 24 with the RMSD as low as 21 m (6.2% nRMSD), with the daily RMSD remaining below 130 m. The daily biases are usually less than 80 m and the overall bias is only 23 m indicating that most of the RMSD is driven by shorter-term random fluctuations that are difficult to model. Also, an unusual day with high cirrus for only two hours was observed on July 1, 2015, so we were able to demonstrate the performance of the method in different conditions. Thin clouds tend to have more diffused edges which may weaken the linear cloud edge assumption and the ability to obtain high correlations between different sensors. Nevertheless, the method still captures the CBH with a RMSD of 830 m that corresponds to an nRMSD of 14.2% given the large CBH. On the other hand, METAR delivers CBH with large differences to local CBH and ceilometer, which demonstrates the spatial variability in cloud coverage due to the climate difference as the METAR site is located 8.8 km further inland, while the CSS is only 1 km from the coastline (These spatial differences would likely be smaller at flat continental sites). In fact, the CSS-USI CBH delivers better CBH than METAR on all days in this study. The proposed CSS+USI method is therefore expected to be superior to METAR CBH in short term solar forecasting.

Note that the sky imager cloud pixel velocity represents all cloud edges in the entire sky image, while the CSS measurement represents a single cloud edge approaching the sun. However, we assume that those two measurements refer to the same cloud edge when applying Eqn. 4 and the effect of the assumption limits the CBH accuracy. In addition, the ceilometer measurement in our validation represents temporally averaged CBH at zenith, while CSS+USI CBH represents spatially averaged CBH. Therefore, random differences between ceilometer CBH and CSS-USI CBH are expected. In summary, the method was generally accurate for low clouds and although it is rare to observe alto-cumulus and cirrus clouds in coastal southern California, May 22 and July 1 confirmed the robustness of the method under those conditions.

Table 1: Daytime average ceilometer, METAR, and CSS-USI cloud base height and difference metrics between ceilometer and CSS+USI. The last line provides the average of the entries in the 27 rows.

Date [YYYYMMDD]	METAR [m]	Ceilometer CBH [m]	$CBH_{CSS+USI}$ [m]	RMSD [m]	nRMSD [%]
2015-04-05	3536	788	848	108	13.7
2015-04-20	793	650	707	76	11.7
2015-05-02	2101	424	490	80	18.9
2015-05-04	1346	782	841	230	29.4
2015-05-10	4577	441	495	73	16.6
2015-05-20	4904	851	1013	170	20.0
2015-05-22	1107	1421	1500	305	21.5
2015-05-29	6631	350	443	100	28.6
2015-06-02	504	450	498	55	12.2
2015-06-04	670	849	948	145	17.1
2015-06-05	740	595	680	145	24.4
2015-06-07	460	359	385	41	11.4
2015-06-16	2840	355	420	80	22.5
2015-06-18	365	288	320	38	13.2
2015-06-25	1759	390	386	30	7.69
2015-07-01	2438	5864	5245	830	14.2
2015-07-03	498	345	398	55	15.9
2015-07-08	708	736	841	200	27.2
2015-07-09	4676	979	976	192	19.6
2015-07-13	374	348	358	22	6.32
2015-07-16	609	494	521	39	7.89
2015-07-17	806	450	452	46	10.2
2015-07-22	965	411	420	117	28.5
2015-07-23	500	415	355	68	16.4
2015-07-24	550	340	332	21	6.21
2015-07-26	470	400	458	73	18.3
2015-07-29	540	444	495	70	15.8
All Days	1683	748	771	126	16.9

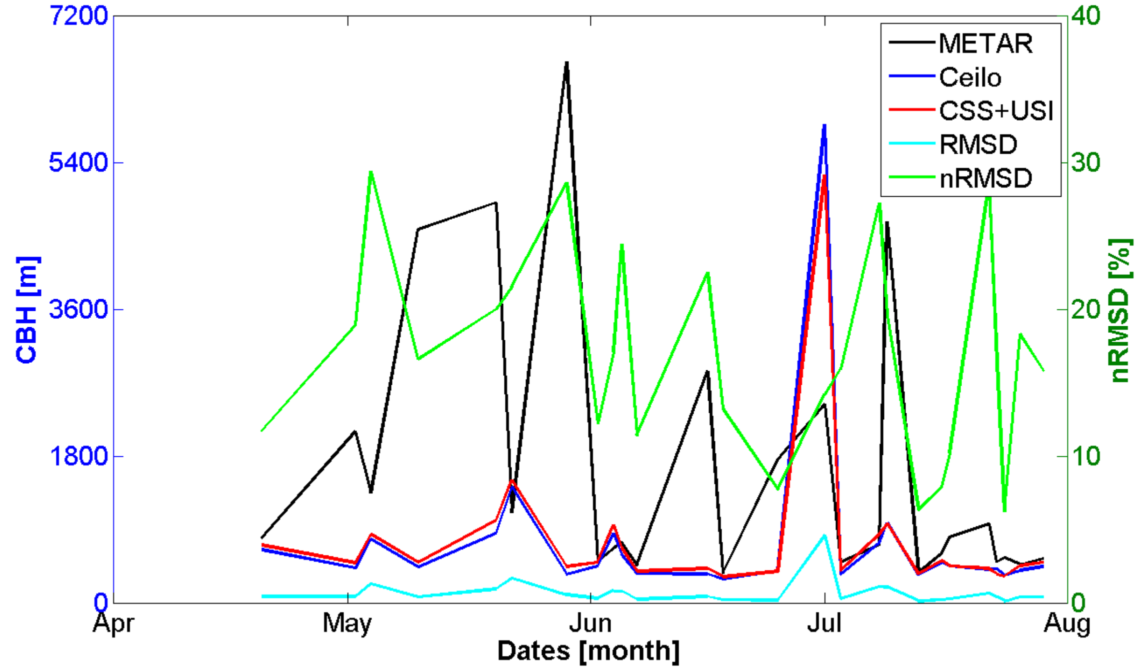

Fig. 9: Comparison of daytime average CBH from METAR, Ceilometer, and CSS+USI. RMSD between CSS+USI and ceilometer are also shown. See Table 1 for detail.

4.2 CBH validation examples for two days

Two detailed examples are analyzed in this section to further illustrate and explain the performance of the CSS+USI method. Fig. 10 shows the CBH comparison of ceilometer measurements, METAR, and the CSS+USI method for May 22, a day with different cloud types and multiple cloud layers. The period from 16:00 to 17:30 UTC is characterized by nearly overcast stratus clouds at 2,000 m AMSL that turn into alto-cumulus at the same altitude. During 18:30-21:45 UTC, scattered cumulus dominate, while after 21:45 UTC, broken cumulus are observed. UTC lags local standard time (PST) by 8 hours.

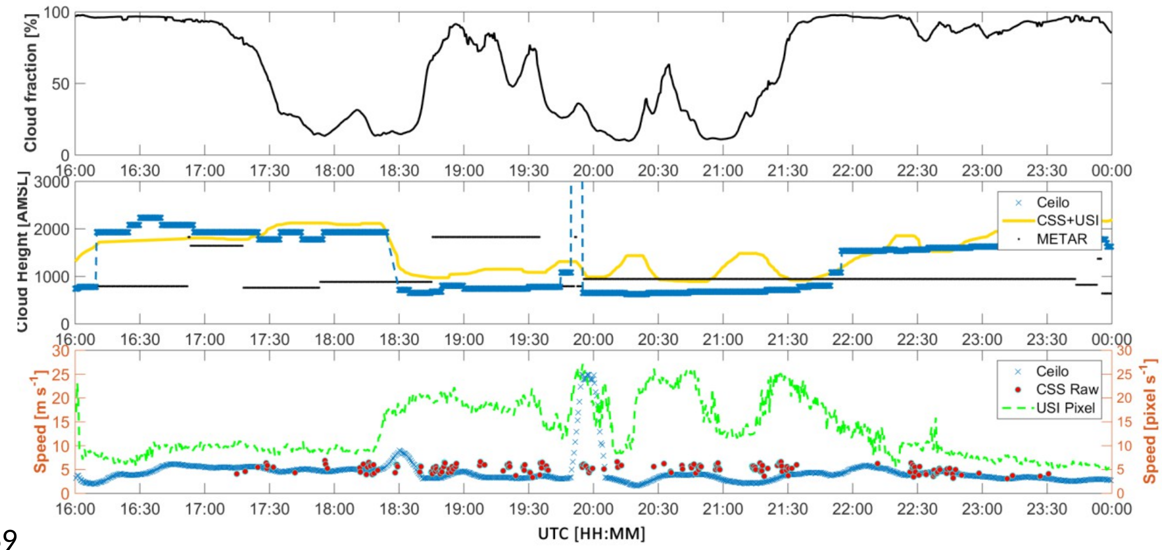

Fig. 10: Sample comparison among different CBH measurements during the daytime of May 22, 2015. See Fig. 2 for locations of the instruments. Top: USI cloud fraction in units of %. Middle: CBH comparison between local ceilometer measurements (blue crosses), and the proposed CSS+USI method described in Section 3 (yellow line). The black dots indicate the measurement from airport METAR at Miramar Naval Air Station (KNKX), 8.8 km to the east of ceilometer. Bottom: Cloud speed determined by the CSS and USI. The green dashed line shows U_{pixel} (right *y*-axis). The blue line represents the cloud speed U_{USI} in m s^{-1} calculated by Eqn. 3 with the CBH input from the local ceilometer measurements, while the red dots show the raw measurements from CSS. The USI pixel speed is not expected to match, but the other two methods are expected to match. Note that the brief period of ~25 m s^{-1} USI+Ceil cloud speed at 20:00 UTC is a result of ceilometer measurements of CBH = 7,500 m which are cut off the middle graph for readability of the CBH variation.

In the middle plot of Fig. 10, both CBH from local ceilometer measurements (the ground truth) and the CSS+USI method yield the same trend. For example, between 16:00-18:30 UTC, the CSS+USI method produces similar CBHs as the local ceilometer at about 2,000 m, while METAR reports 800 m which substantiates the concerns about using off-site METAR CBH data. At 18:30 UTC, ceilometer measurements indicate a CBH transition from about 2,000 m to 750 m, and the CBH from the CSS+USI method follows this transition, although with about a 300 m offset. After 20:00 UTC, an additional cloud layer with a different direction and variable speed, temporarily confuses the $CBH_{CSS+USI}$, as evident in a briefly elevated CBH around 20:15 UTC, 21:15 UTC and 22:15 UTC. However, the CSS+USI method still captures the CBH transition detected by the ceilometer from 800 m to 1,500 m at 22:00 UTC, and follows the ceilometer measurement until the end of the day. Again, METAR CBHs differ after 22:00 UTC indicating spatial heterogeneity in CBH. In summary, the CSS+USI method is accurate on this day especially in the morning. The daily RMSD is 305 m and nRMSD is 21.5%.

July 8 is analyzed in Fig. 11 as an example of a day with one of the largest observed nRMSD (27.2%). On this day, there are unusual fluctuations in cloud pixel speed reported from 19:30 UTC to 22:00 UTC, especially a brief period of significantly smaller pixel speeds around 20:30 UTC, which causes a large CBH peak at that time. Visual inspection of the cloud images indicates that these fluctuations are not representative of the actual cloud motion, though the exact reason that the USI motion algorithm performs poorly is unclear. Regardless, this illustrates again that the accuracy of the CBH estimate depends on the quality of cloud vectors from both the USI and the CSS.

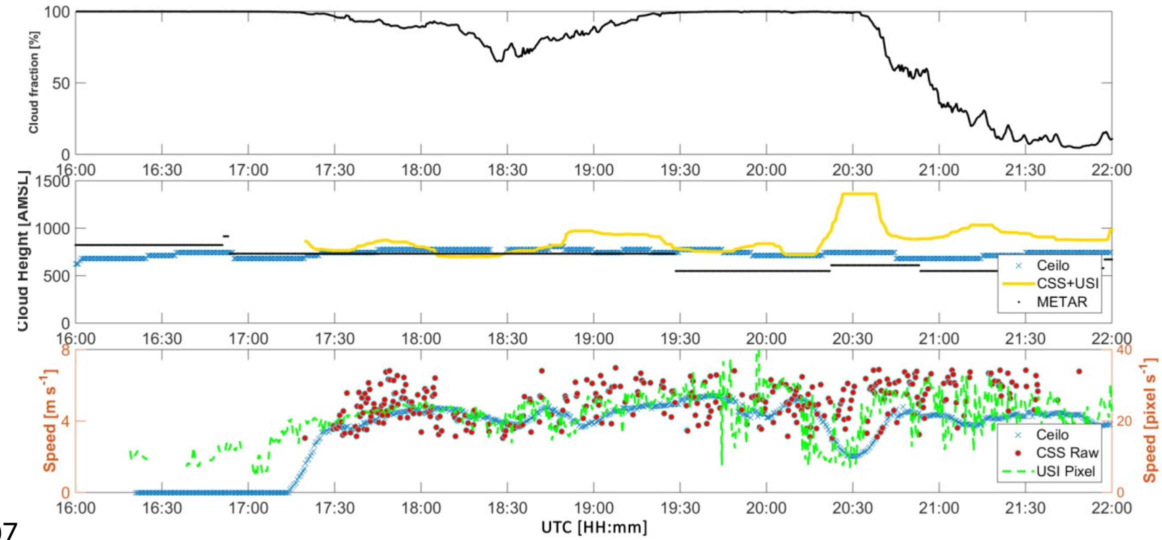

Fig. 11: Same as Fig. 10, but for July 8 illustrating a case when unstable cloud pixel speed determination causes a large offset of local CBH estimates.

4.3 Assumptions and limitations

In this section, the improvement and possible reasons for CBH errors are further discussed. Its performance is further compared to a prior method introduced by Bosch et al. (2013).

As implemented in section 3.2, the LCE assumption implies that only the component of the velocity that is perpendicular to the cloud edge is detected. This assumption can cause offsets in determining CMVs, which is illustrated in Fig. 12. The cloud edge initially shades the central sensor at $t=t_0$, and then moves in one of two ways until it shades sensor 6. (i) It moves perpendicular to the cloud edge with speed v_1 and reaches sensor 6 at $t=t_1$, which is consistent with LCE assumption. (ii) It moves in a non-perpendicular direction with speed v_2 whose component normal to the cloud edge is v_1, and also reaches sensor 6 at $t=t_1$. In these two cases the signal measured by sensor 6 would be identical. Therefore, no matter what the direction of the CMV, the LCE-CFM will only detect the cloud speed component perpendicular to the cloud edge (here v_1). Thus, if the CMV is not perpendicular to the cloud edge, the cloud speed is underestimated, and subsequently, the lower CSS measurements causes a lower local CBH according to Eqn. 4. This is the main limitation of the linear cloud edge assumption.

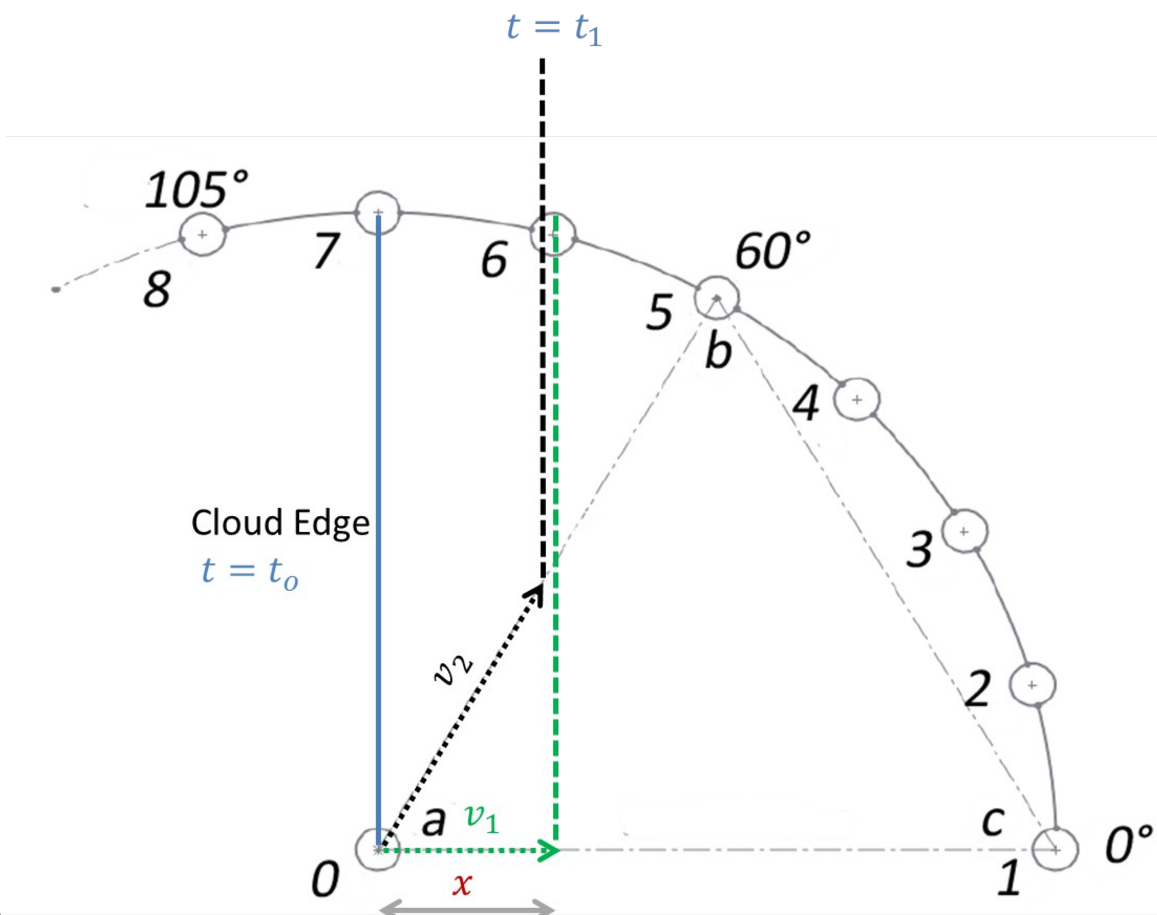

Fig. 12: Illustration of a thought experiment that shows LCE-CFM method can only measure the velocity component perpendicular to the cloud edge due to a limitation of the linear cloud edge assumption. The blue line represents the original cloud edge and the vertical green dashed line represents the future position associated with the CMV v_1, while the black line indicates the future position associated with the CMV v_2.

For an infinite linear cloud edge, the cloud positions resulting from v_1 and v_2 in Fig. 12 are indistinguishable, while for real (finite) clouds, the cloud positions will be different. Bosch et al. (2013) addressed this ambiguity by assuming that successive clouds passing the sensor move with the same CMV as they are transported by air at the same height in the boundary layer. Two successive clouds that pass the sensor array with CMV v_{real} and different edge orientations will record velocities $v_{\perp_1}$ and $v_{\perp_2}$, at angles $\phi_{\perp_1}$ and $\phi_{\perp_2}$ as shown in Fig. 13. The true velocity v_{real}, can then be found as:

$$|v_{real}| = \frac{|v_{\perp_1}|}{\cos(\phi_{\perp_1} - \beta)} = \frac{|v_{\perp_2}|}{\cos(\phi_{\perp_2} - \beta)} \quad , \qquad (6)$$

which requires the angle of the true velocity, β :

$$\tan\beta = \frac{-|v_{\perp_1}|\cos(\phi_{\perp_2}) - |v_{\perp_2}|\cos(\phi_{\perp_1})}{|v_{\perp_1}|\sin(\phi_{\perp_2}) - |v_{\perp_2}|\sin(\phi_{\perp_1})} \quad . \qquad (7)$$

However, as can be seen in Eqns. (6) and (7), v_{real} and β are sensitive to noise when $\phi_{\perp_1}$ is approximately equal to $\phi_{\perp_2}$. We have therefore opted to leave a more complete implementation of this method as future work. For the present analysis, we assume v_{real} = $v_{\perp_1}$ = $v_{\perp_2}$ and use temporal averaging of motion vectors. This is expected to produce approximately correct direction vectors, since detected velocities are distributed about v_{real} , but systematically underestimates the speed (vector magnitude) slightly, because all potential $v_{\perp}$ are shorter than v_{real} . The underestimation varies quantitatively depending on the cosine of the cloud edge orientation bias as per Eqn. 6.

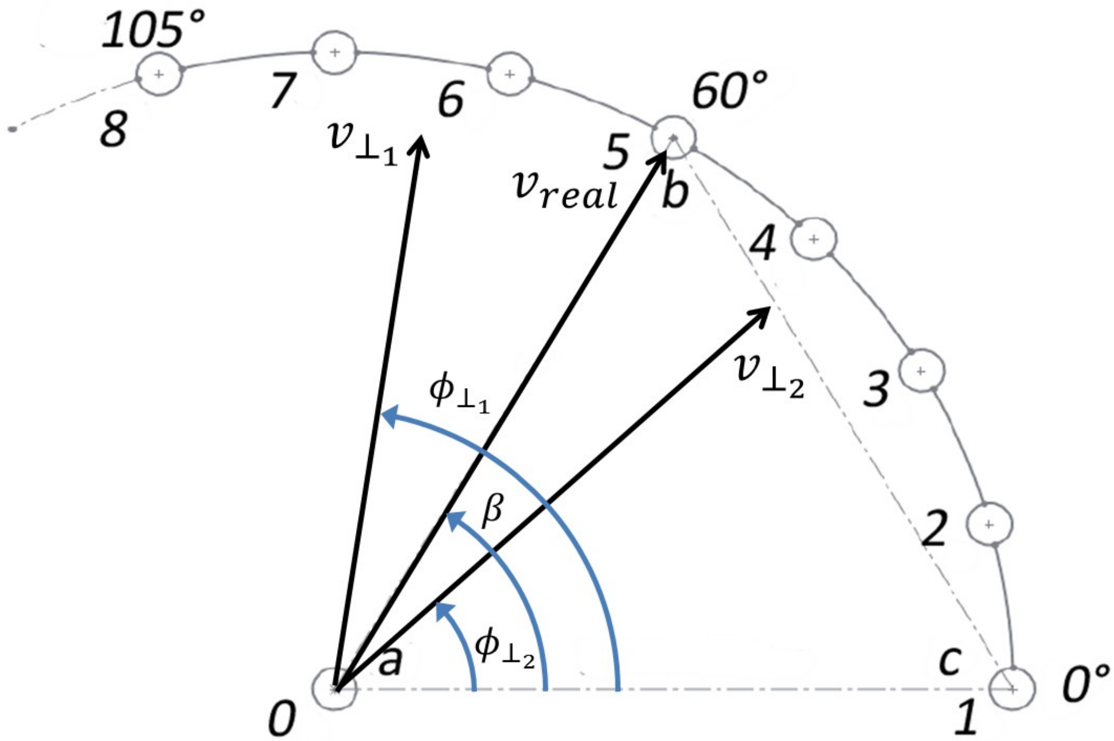

Fig. 13: Determining real cloud velocity from perpendicular components. v_{real} is real cloud speed with angle of β in reference to horizontal line (a-c). $v_{\perp_1}$ and $v_{\perp_2}$ are the CMVs perpendicular to the detected cloud edge from two different passing clouds, and their angles are $\phi_{\perp_1}$ and $\phi_{\perp_2}$ in reference to line (a-c), respectively.

The original LCE method was developed by Bosch et al. (2013) for a sensor triplet in any non-linear configuration and spacing and CMVs are solved by geometric-kinematic equations based on the cloud arrival time at different sensors. While the sensor setup differs, the basic kinematic analysis of the original LCE method and the LCE-CFM that relies on LCE assumption is similar; a linear cloud edge passes over the sensors and causes different arrival times based on sensor arrangements relative to the CMVs. But two main differences do exist between two methods. i) The original LCE method develops equations to solve two unknowns–speed and direction—using two data points. In contrast, the LCE-CFM uses 12 data points to solve for the same two unknowns. The resulting system is over-defined and therefore more tolerant to signal noise. This also explains why the original LCE method requires low noise signals and multiple quality controls to produce less scattered results but the LCE-CFM has more clustered CMV raw measurements without post-filtering. ii) As discussed above, the original LCE method provides a mechanism to account for the impact of CMV not being perpendicular to the cloud edge, while the LCE-CFM method returns the CMV perpendicular to the cloud edge. The difference is summarized in Table 2.

Table 2: Performance comparison between the original LCE and proposed LCE-CFM method.

	Original LCE	LCE-CFM
CMV distribution	High noise and scattered raw data	Low noise and clustered raw data
CMV limitation	None	Detect the CMV only perpendicular to the cloud edge

5. Discussion and Conclusions

The principal objective of this research is to introduce a combination of sensors and an algorithm to provide an accurate local CBH for sky imager solar forecasting. The combination of a cloud speed sensor and sky imager makes measurements of CBH more affordable and convenient compared to a ceilometer. Ceilometers cost about US$20k while the bill of materials for the CSS is less than US$400. Furthermore, a CSS could be directly integrated into the enclosure of a sky imager avoiding the need for a separate setup site, power and Ethernet connectivity. In contrast, a ceilometer is bulky and requires separate infrastructure.

Firstly, the linear cloud edge assumption of Bosch et al. (2013) is leveraged to propose a method (LCE-CFM) for CSS measurements. The method analyzes the similarity, i.e. the correlation, of luminance signals between pairs of sensors aligned in different directions. Unlike the original CSS method that only considered the time delay of the most correlated pair, all 12 pairs of sensors are utilized to fit a cosine function of cross-correlation time delay versus sensor pair direction. The approach is motivated by assuming a linear cloud edge passing over the array of sensors. If a good fit is observed, the cloud direction is determined as the angle with the maximum time delay of the cloud passage on the cosine curve fit. The cloud speed is then equal to the sensor spacing divided by that time delay. The advantages and limitations of the LCE-CFM are illustrated. The method is also compared to a prior LCE method proposed by Bosch et al. (2013).

CBH is derived by comparing CSS cloud speed measurements in [m s^{-1}] to cloud pixel speed in [pixel s^{-1}] from a single sky imager. Over 27 days, the CSS+USI method shows promising CBH results with average RMSD of 126 m and nRMSD of 16.9% compared to on-site ceilometer measurements. The CBH accuracy depends on the accuracy of both the CSS cloud speed and the USI cloud pixel speed, as well as their mutual agreement. While the cloud pixel velocity is identified based on CMVs in the entire sky image, the CSS measures the CMVs just of the clouds approaching the sun. This discrepancy limits the CBH accuracy. Also, multiple layers of cloud with different direction and/or speed could degrade the performance because both CSS and USI are only able to determine cloud speed of a single cloud layer. In addition, the accuracy is restricted by the fact that the linear cloud edge assumption requires that the cloud motion vector be perpendicular to the cloud edge, which causes an underestimation of cloud speed. Lastly, the validation suffers from inconsistent measurement areas: (i) the ceilometer measures clouds straight overhead, (ii) the CSS detects the clouds that obscure the sun, and (iii) the USI analyzed clouds within its field of view that is typically about 10 km^2. This could result in inconsistencies between the ceilometer and the CBH from the CSS+USI method.

Future efforts will focus on implementation of real cloud velocity estimates from perpendicular components of two different passing cloud edges. USI cloud speed detection could also be improved. For example, a CMV field derived from optical flow (Chow et al. 2015) could provide the localized information to associate the CMV of the cloud passing the CSS. Optical flow also enables detection of multiple cloud layers as well as their respective cloud pixel speeds. Finally, validation under different meteorological conditions more relevant to continental climates would further substantiate the general applicability of the method.

Acknowledgements

We acknowledge the donation of a ceilometer from Lawrence Livermore National Laboratory facilitated by Julie Lundquist. We also thank Victor Fung, Juan Luis Bosch, and Dominic Fong for assisting with CSS maintenance and operation. Juan Luis Bosch suggested the analysis in Appendix A1.

Appendix A1: Validation of the LCE method

Fig. A-1 illustrates the direction offset between the direction of 0 s time shift ($\Delta t_{ij}=0$) and the direction that is determined by the LCE-CFM. For example, in Fig. 4, the direction determined by the LCE-CFM method is 322.7°, while the direction closest to 0 s time shift is 240°, so the offset is -82.74°. Under the LCE assumption, these two directions should always be at right angles to each other; if the cloud edge is not linear, the offset will be larger or smaller depending on the shape of the cloud edge. The calculation is applied to all 27 days analyzed in this paper and the results are plotted in form of histogram in Fig. A-1. Most of the angle offsets are clustered around -90° and +90° which indicates that the data are consistent with the LCE assumption.

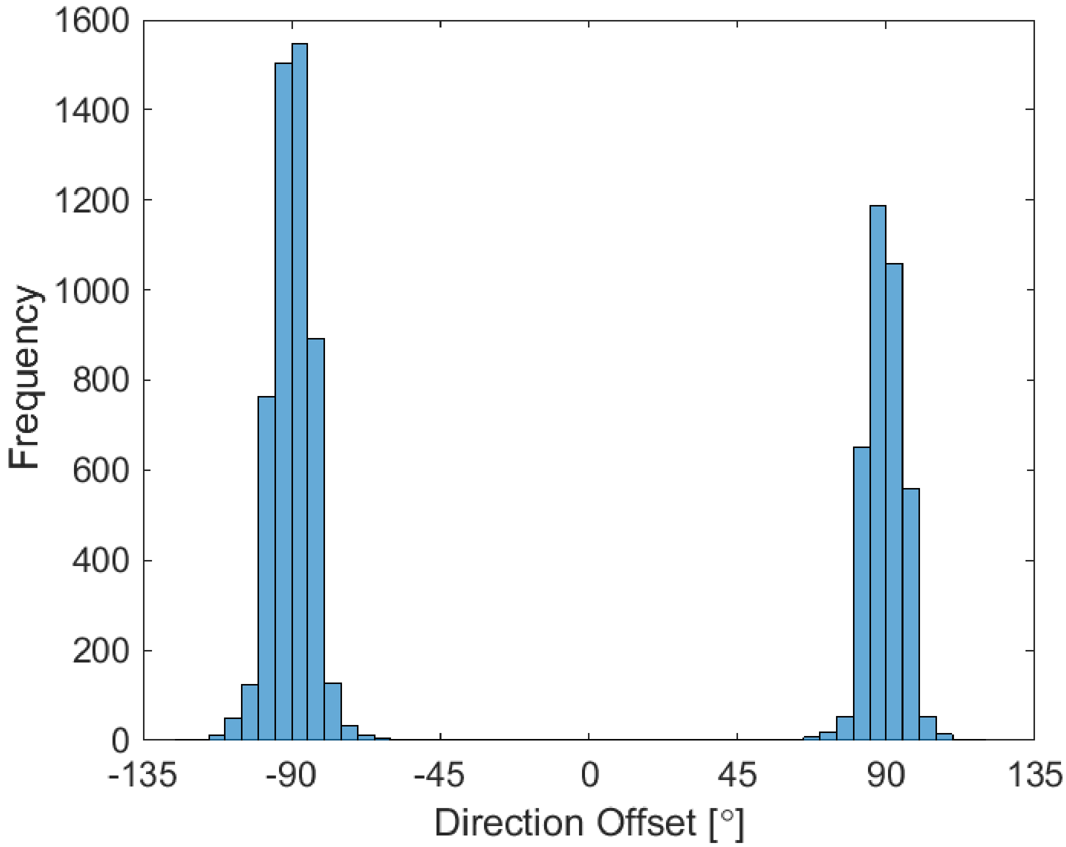

Fig. A-1: Histogram of LCE assumption validation on all 27 days analyzed in this paper. The *y*-axis represents the number of CMVs determined by the LCE-CFM using 9-sec segments of CSS data, and the *x*-axis represents angle offsets between the cloud direction from the LCE-CFM and the direction from the sensor pair which has a time shift closest to zero.

Appendix A2: Prior MCP method performance

Fig. A-2 illustrates that the prior MCP method suffers from some deficiencies as a result of arbitrary correlations from sensor noise, resulting in scattered CMVs outputs. Filtering can address the CMVs variability issue, but at the same time reduces the response of the sensor to sudden changes in cloud velocity. Also, the cloud direction outputs are not continuous as the final direction can only lie along individual sensor pairs.

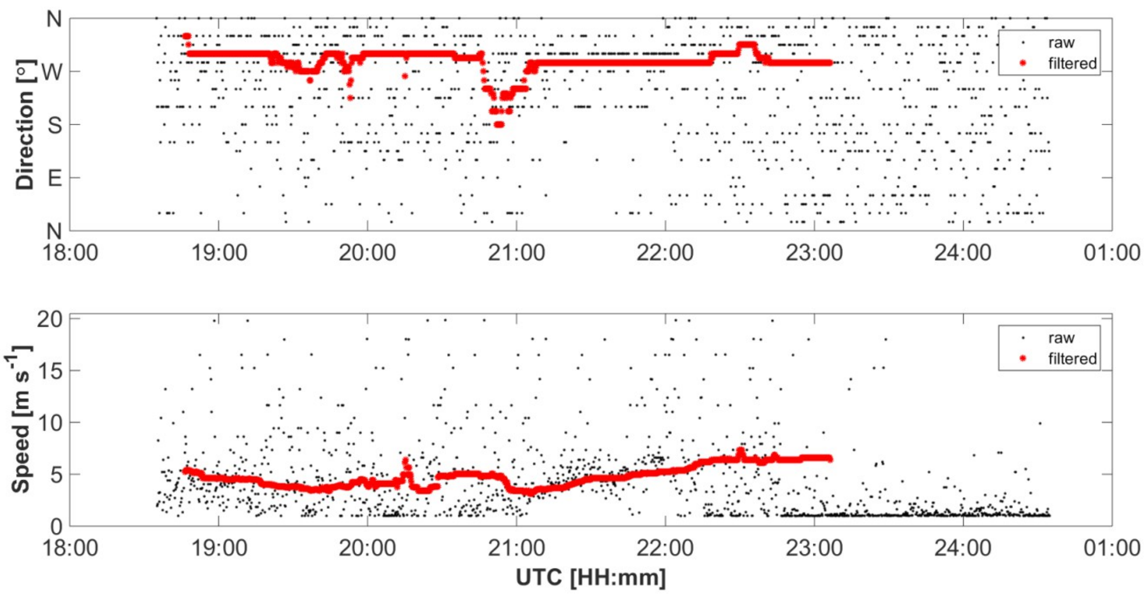

Fig. A-2: An example of the MCP method on July 24, 2013. Black dots show the raw measurement, and red dots show the filtered measurements after moving median filtering.

5528
56

Appendix A3: Pseudocode

The pseudocode and flowchart (Fig. A3) that show the steps involved to determine local CBH is listed in this section. All acronyms used in pseudocode and flowchart are defined in Table A-3. For the cases when the USI or the CSS output a NaN CMV, or the CSS outputs a CMV that deviates more than 60 ° from the USI CMV, the algorithm will deliver a NaN CBH. Refer to section 3.2 for the frequency with which NaN CMV is delivered by CSS. The chance that the USI outputs a NaN CMV is only about 3% for partly cloudy days. Since CBH typically changes slowly for conditions with one cloud layer an average of recent results could be used in place of $CBH_{CSS+USI} = NaN$.

Table A-3: Definition of acronyms used in pseudocode and flowchart. USI is UCSD Sky Imager and CSS is Cloud Shadow Speed Sensor.

$CBH_{CSS+USI}$	CBH derived from CSS measurements and USI cloud pixel speed	USI_{dir}	USI derived cloud direction
CSS_{speed}	CSS measured cloud speed	USI_{pixel}	USI derived cloud pixel speed
CSS_{dir}	CSS measured cloud direction	USI_{speed}	USI derived cloud speed
n	Number of pixels of the cloud map in one dimension	θ_m	Field of view of the USI in degrees from the vertical

Fig. A-3: Flowchart for CBH determination from sky imager and cloud speed sensor.

Flowchart	Pseudocode

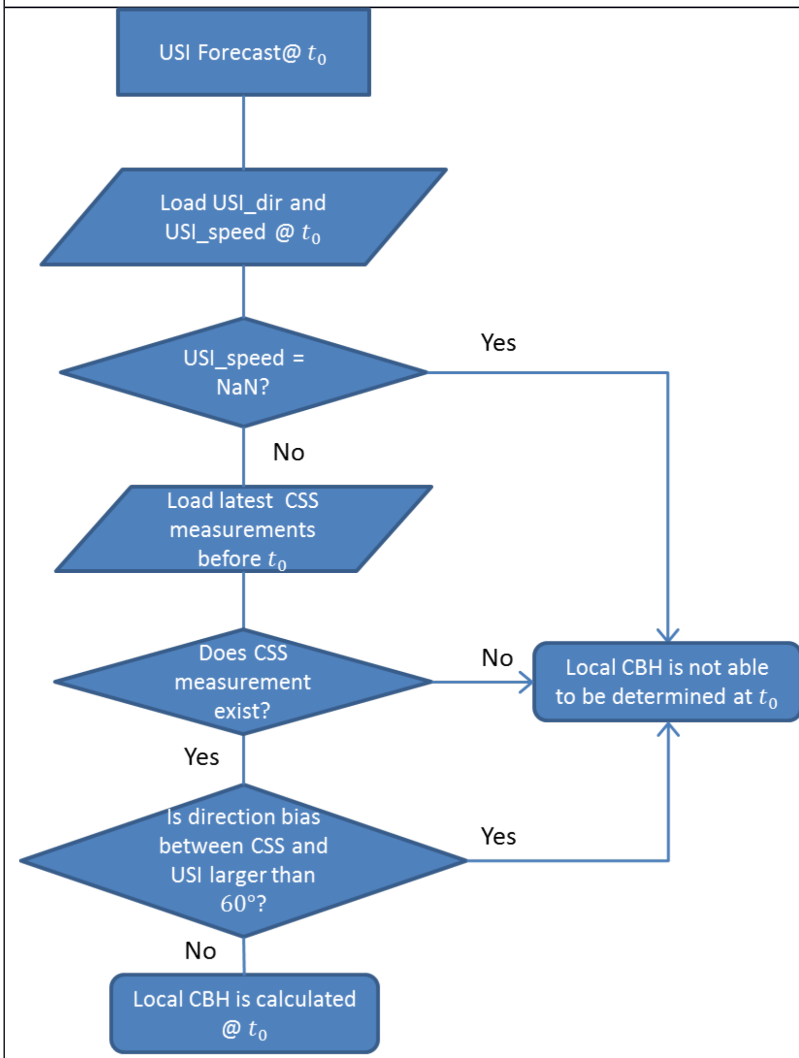

USI forecast algorithm runs to timestamp t_0

Load USI cloud motion vector at time step t_0

If ($USI_{speed}=NaN$)

$CBH_{CSS+USI}=NaN$;

Else

Load the latest CSS cloud velocity measurement before time step t_0

If ($CSS_{speed}=NaN$)

$CBH_{CSS+USI}=NaN$;

Else If

(| $CSS_{dir}-USI_{dir}\vee¿60°¿$

$CBH_{CSS+USI}=NaN$;

Else

$CBH_{CSS+USI}=\frac{CSS_{spee}}{USI_{pixel}\times}$

;

End

End

Move to next timestamp.

731

6131
62

References

Allmen, M. C., & Kegelmeyer Jr, W. P. (1996). The computation of cloud-base height from paired whole-sky imaging cameras. *Journal of Atmospheric and Oceanic Technology, 13(1), 97-113*.

Bosch, J., & Kleissl, J. (2013). Cloud motion vectors from a network of ground sensors in a solar power plant. *Solar Energy, 95, 13-20*.

Bosch, J. L., Zheng, Y., & Kleissl, J. (2013). Deriving cloud velocity from an array of solar radiation measurements. *Solar Energy, 87, 196-203*.

Bosch JL, Kleissl J. (2013). Cloud motion vectors from a network of ground sensors in a solar power plant, *Solar Energy, 95, 13-20*.

Bright, J., Smith, C., Taylor, P., & Crook, R. (2015). Stochastic generation of synthetic minutely irradiance time series derived from mean hourly weather observation data. *Solar Energy, 115, 229-242*.

Cazorla Cabrera, A. (2010). Development of a sky imager for cloud classification and aerosol characterization. Universidad de Granada.

Chow, C. W., Belongie, S., & Kleissl, J. (2015). Cloud motion and stability estimation for intra-hour solar forecasting. *Solar Energy, 115*, 645-655.

Chow, C. W., Urquhart, B., Lave, M., Dominguez, A., Kleissl, J., Shields, J., et al. (2011). Intra-hour forecasting with a total sky imager at the UC San Diego solar energy testbed. *Solar Energy, 85(11), 2881-2893*.

Dessler, A., Palm, S., & Spinhirne, J. (2006). Tropical cloud-top height distributions revealed by the ice, cloud, and land elevation satellite (ICESat)/Geoscience laser altimeter system (GLAS). *Journal of Geophysical Research: Atmospheres (1984–2012), 111*(D12)

Fung, V., Bosch, J., Roberts, S., & Kleissl, J. (2014). Cloud shadow speed sensor. *Atmospheric Measurement Techniques, 7(1), 1693-1700*.

Gaumet, J., Heinrich, J., Cluzeau, M., Pierrard, P., & Prieur, J. (1998). Cloud-base height measurements with a single-pulse erbium-glass laser ceilometer. *Journal of Atmospheric and Oceanic Technology, 15*(1*), 37-45*.

Ghonima, M., Urquhart, B., Chow, C., Shields, J., Cazorla, A., & Kleissl, J. (2012). A method for cloud detection and opacity classification based on ground based sky imagery. *Atmospheric Measurement Techniques, 5(11), 2881-2892*.

Kassianov, E., Long, C. N., & Christy, J. (2005). Cloud-base-height estimation from paired ground-based hemispherical observations. *Journal of Applied Meteorology, 44(8), 1221-1233*.

Killius, N., Prahl, C., Hanrieder, N., Wilbert, S., & Schroedter-Homscheidt, M. (2015) *On the use of NWP for Cloud Base Height Estimation in Cloud Camera-Based Solar Irradiance Nowcasting. ICEM 2015, 23.-26. June 2015, Boulder, USA.*

Liu, L., Sun, X., Liu, X., Gao, T., & Zhao, S. (2015). Comparison of cloud base height derived from a ground-based infrared cloud measurement and two ceilometers. *Advances in Meteorology.*

Martucci, G., Milroy, C., & O'Dowd, C. D. (2010). Detection of cloud-base height using jenoptik CHM15K and vaisala CL31 ceilometers. *Journal of Atmospheric and Oceanic Technology, 27(2), 305-318*.

Nguyen, D. A., & Kleissl, J. (2014). Stereographic methods for cloud base height determination using two sky imagers. *Solar Energy, 107, 495-509*.

Prata, A., & Turner, P. (1997). Cloud-top height determination using ATSR data. *Remote Sensing of Environment, 59(1), 1-13*.

Schmidt, T., Kalisch, J., Lorenz, E., & Heinemann, D. (2015). Evaluating the spatio-temporal performance of sky imager based solar irradiance analysis and forecasts. *Atmospheric Chemistry and Physics Discussions, 15(19), 26997-27039*.

Shaw, J. A., & Nugent, P. W. (2013). Physics principles in radiometric infrared imaging of clouds in the atmosphere. *European Journal of Physics, 34(6), S111–S121*.

Urquhart, B., Kurtz, B., Dahlin, E., Ghonima, M., Shields, J., & Kleissl, J. (2015). Development of a sky imaging system for short-term solar power forecasting. *Atmospheric Measurement Techniques, 8, 875-890*.

Wang, J., & Rossow, W. B. (1995). Determination of cloud vertical structure from upper-air observations. *Journal of Applied Meteorology, 34(10), 2243-2258*.

Yang, H., Kurtz, B., Nguyen, D., Urquhart, B., Chow, C. W., Ghonima, M., et al. (2014). Solar irradiance forecasting using a ground-based sky imager developed at UC San Diego. *Solar Energy, 103, 502-524*.